Modeling Specular Exchange between Concentric Cylinders in a Radiative Shielded Furnace

R. Gregory Schunk
NASA Marshall Space Flight Center
Thermal and Fluid Systems Group

and

Francis C. Wessling
Department of Mechanical and Aerospace Engineering
University of Alabama in Huntsville

INTRODUCTION

The objective of this research is to develop and validate mathematical models to characterize the thermal performance of a radiative shielded furnace, the University of Alabama in Huntsville (UAH) Isothermal Diffusion Oven. The mathematical models are validated against experimental data obtained from testing the breadboard oven in a terrestrial laboratory environment. It is anticipated that the validation will produce math models capable of predicting the thermal performance of the furnace over a wide range of operating conditions, including those for which no experimental data is available. Of particular interest is the furnace core temperature versus heater power parametric and the transient thermal response of the furnace. Application to a microgravity environment is not considered, although it is conjectured that the removal of any gravity dependent terms from the math models developed for the terrestrial application should yield adequate results in a microgravity environment.

The UAH Isothermal Diffusion Oven is designed to provide a thermal environment that is conducive to measuring the diffusion of high temperature liquid metals. In addition to achieving the temperatures required to melt a sample placed within the furnace, reducing or eliminating convective motions within the melt is an important design consideration [1]. Both of these influences are reflected in the design of the furnace. Reducing unwanted heat losses from the furnace is achieved through the use of low conductivity materials and reflective shielding. As

evidenced by the highly conductive copper core used to house the sample within the furnace, convective motions can be greatly suppressed by providing an essentially uniform thermal environment. An oven of this design could ultimately be utilized in a microgravity environment, presumably as a experiment payload. Such an application precipitates other design requirements that limit the resources available to the furnace such as power, mass, volume, and possibly even time. Through the experimental and numerical results obtained, the power requirements and thermal response time of the breadboard furnace are quantified.

A series of laboratory tests are conducted to measure the steady state and transient behavior of the furnace. To aid in the model correlation, the test conditions are chosen to isolate or enhance specific aspects of the thermal behavior of the furnace. Under vacuum, radiative exchange is the dominant heat transfer mechanism. At very low pressure, natural convection is suppressed and, along with radiation, gaseous conduction significantly influences the thermal performance of the furnace. Near atmospheric pressure, all three heat transfer modes, convection, conduction, and radiation, must be considered to adequately characterize the thermal behavior of the furnace. The test conditions are also chosen to parameterize the furnace core temperature versus heater power and to observe the influence of natural convection over a range of pressures. Actual testing of a sample within the furnace is excluded since the heat capacity of the sample is considered negligible relative to that of the core.

Development of math models to characterize the thermal behavior of the furnace is a challenging task due to the complexity of the interacting heat transfer modes as well as other factors related to the design of the furnace. Important considerations in the analysis of the furnace include heat losses through power and instrumentation cables, buoyancy driven flows through and around exposed surfaces of the furnace, and specular radiation effects within the furnace. In the model, a network representation of the furnace is developed where individual nodes represent discretized portions of the furnace or the boundary and the heat transfer is proportional to the temperature difference between nodes. Empirical relations are used to model free convection

from the exposed surfaces of the furnace while a one-dimensional compressible flow model is developed to quantify the losses resulting from a buoyancy driven flow through the furnace. Specialized models to account for the fin effect heat losses from exposed cables and instrumentation are also developed as well as models to quantify the impact of specularly reflecting surfaces within the furnace.

FURNACE DESIGN

A cross-sectional view of the oven is presented in Figure 1 with major components noted [2]. A cylindrical copper core and a quartz glass tube are used to house the test sample. The quartz glass tube and sample are absent in the breadboard furnace that is considered in this research. It is assumed that the thermal behavior of the furnace can be adequately characterized without the tube and sample since the heat capacities of these components are negligible compared to that of the copper core. The copper core is surrounded by a cylindrical boron nitride sleeve containing a graphite heater element [3,4]. A thin layer of Fiberfrax™ insulation is used to enhance the heat transfer between the core and the concentric heater element. Two stainless steel end hubs, denoted long and short in the figure, are attached to opposite ends of the copper core [5,6]. The top and bottom hubs contain four and six pins, respectively, that mate with matching penetrations in each end of the copper core. Fiberfrax™ gaskets are introduced between the hubs and the core to minimize heat losses and, thus, reduce axial temperature gradients through the core. The inner assembly (including core, sample, heater, and insulation) is suspended inside of the oven by stainless steel wires fastened between the two hubs and the top and bottom support rings. The stainless steel wires penetrate each of the interior end rings. Conduction from the core to the end rings is minimized by wrapping the stainless steel wire with Fiberfrax™ insulation within the penetrations. The overall design goal is to provide a stable and secure mount for the inner assembly while minimizing heat losses to the outside.
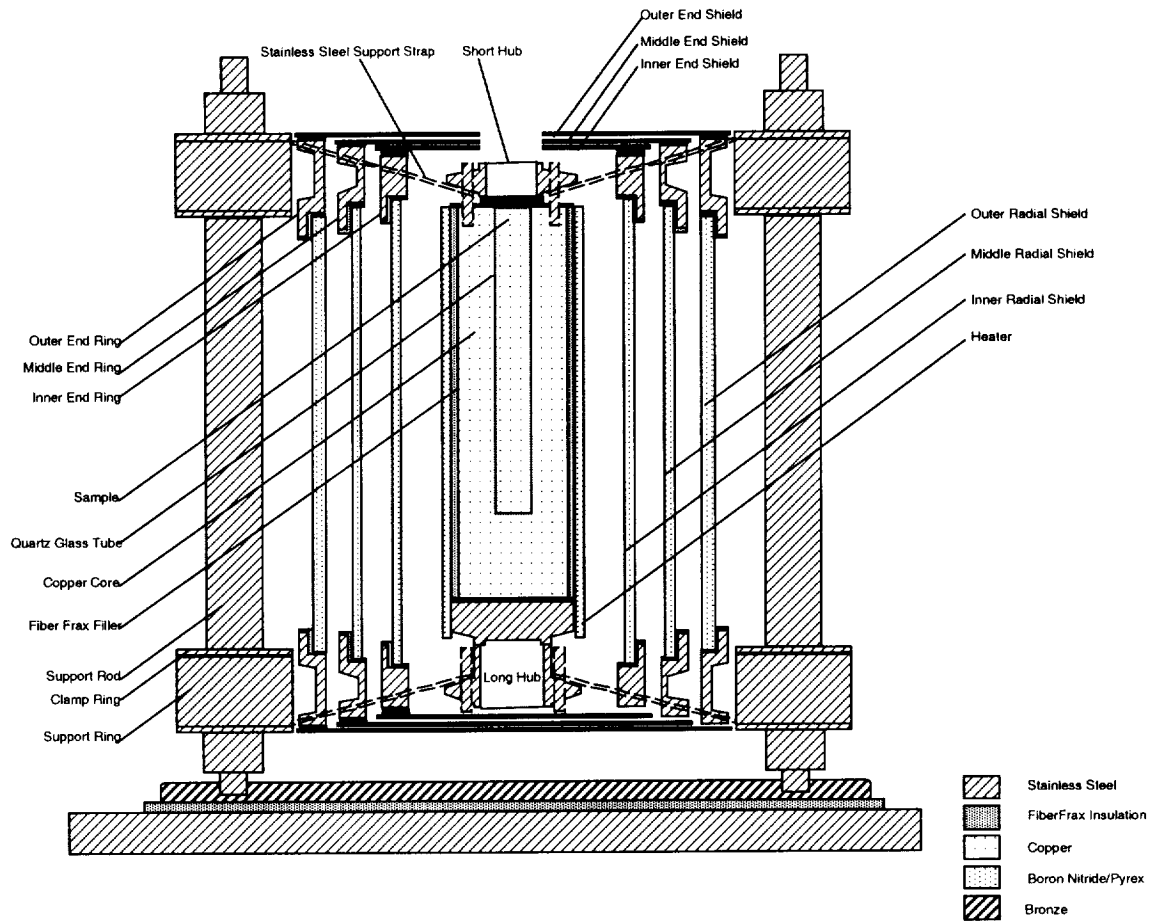
Figure 1 UAH Isothermal Diffusion Oven

Three cylindrical radial shields (inner, middle, and outer) form a radiation barrier to reduce heat losses from the oven (although gaseous conduction is also present if the furnace is not placed in a vacuum) [7,8,9]. The inner surface of each radial shield has a vacuum deposited low emittance gold coating. The shields are constructed from Pyrex™ and the outer surfaces are uncoated. Visual inspection of the radial shields reveals that the inner surfaces are highly specular. The spacings between the three shields and the core are minimized to suppress convective exchange between the shields and to reduce specular losses from reflected energy escaping out the ends of the furnace. Each radial shield is supported by a matching pair of end rings on the opposite ends (top and bottom). At each end, Fiberfrax™ spacers are used to create a

gap between the radial shield and the end ring. Similarly, Fiberfrax™ washers are used to create a gap between the end rings and the end shields. The gaps reduce the direct contact area between the shields and the end rings and effectively limit the heat exchange to the energy that can be radiated and conducted (through the gaseous medium) across the gap. Like the radial shields, the three shields on each end of the oven form a radiation barrier to reduce heat leakage although the end shields on top of the furnace have a circular penetration to permit loading of the test sample (not used in the experiments) [10,11,12]. The lower end shields are made of stainless steel while the upper shields are aluminum and are polished as needed to remove accumulated oxidation (to create surfaces with as low an infrared emittance as possible). Three support rods hold the entire assembly together and are used to mount the oven onto a bronze baseplate containing a matching hole pattern. The oven and bronze baseplate are placed within a bell jar vacuum chamber for the experiments.

Photographs of the disassembled furnace are contained in Figures 2 and 3. The first figure shows the bare copper core mounted atop the long hub on the bottom end ring assembly. The inner and middle radial shields are removed as well as the top end ring assembly containing the short hub, top support rings, and top end rings. The short hub and stainless steel support wires are visible within the top end ring assembly. The compact design of the oven is evidenced from a six inch scale included in the photograph.

The second figure shows the inner assembly (core and heater sleeve) mounted within the disassembled furnace. The long hub is obscured by the boron nitride heater sleeve which surrounds the core. Penetrations within the heater sleeve that are used to attach power cables are visible in the photograph. Although not visible, the power cables are routed through penetrations underneath the furnace. The support rods, which hold the entire assembly together, are shown in the figure. The end shields, which attach directly to the end rings, are omitted from both photographs.
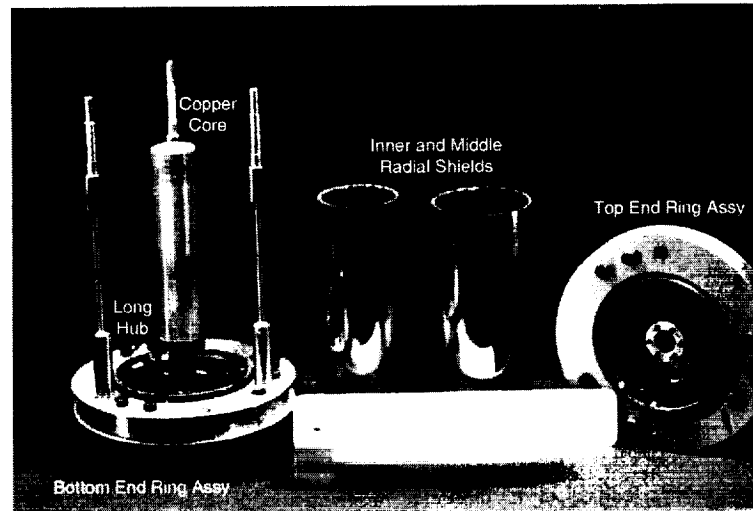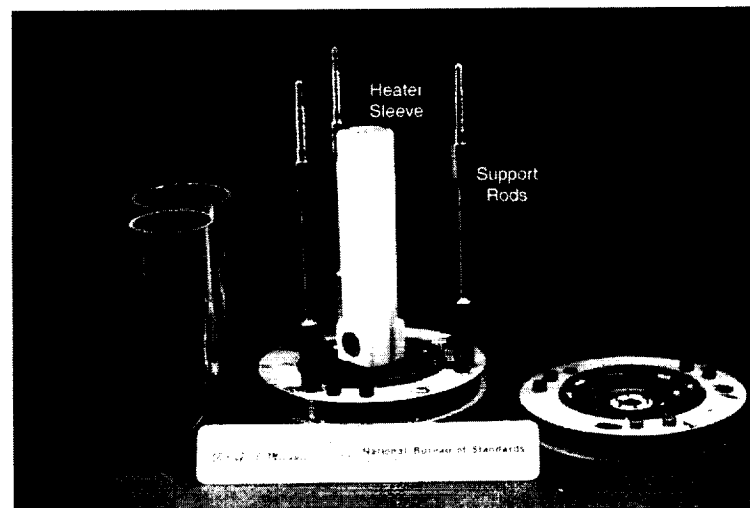
Figure 2 Disassembled View of the Furnace

Figure 3 Furnace with Heater Sleeve

TESTING

Eight tests are conducted under vacuum and varying pressures of argon gas to measure the steady state and transient thermal performance of the furnace. Results from the tests are used to validate mathematical models of the furnace. To aid in the model correlation, the test conditions are chosen to isolate or enhance specific aspects of the thermal behavior of the furnace. Under vacuum, radiative exchange between the furnace core and radial shields is the dominant heat transfer mechanism. At very low pressure, natural convection is suppressed and,

along with radiation, gaseous conduction between the core and radial shields significantly influences the thermal performance of the furnace. Near atmospheric pressure, all three heat transfer modes, convection, conduction, and radiation, must be considered to adequately characterize the thermal behavior of the furnace. The results from the eight tests are summarized in Table 1. The first three tests are conducted under vacuum at power levels ranging between 5 and 20 watts. The final five tests are conducted under absolute pressures of argon gas ranging from 0.03 to 0.932 atmospheres at power levels between 11.6 and 12.0 watts.

Table 1 Steady State Test Results

Test	Date	Core (°C)	Radial #1 (°C)	Radial #3 (°C)	End (°C)	Chamber (°C)	Room (°C)	Voltage (volts)	Current (amps)	Power (watts)	Pressure (torr/atm)
1	12/13/95	390.6	268.7	43.2	113.0	25.3	24.7	12.2	0.92	11.2	3.90E-05 torr
2	12/15/95	262.9	170.9	34.6	72.1	27.2	27.1	8.6	0.60	5.2	8.60E-06 torr
3	12/30/95	506.5	368.1	56.2	153.2	22.8	22.7	19.0	1.06	20.1	3.60E-05 torr
4	1/20/96	201.5	121.3	45.9	53.7	23.5	23.0	11.6	1.00	11.6	0.667 atm
5	2/10/96	219.4	135.1	52.0	63.5	23.6	23.5	11.9	1.00	11.9	0.310 atm
6	2/12/96	228.0	143.4	60.1	72.1	28.4	28.3	12.0	1.00	12.0	0.146 atm
7	2/19/96	203.1	118.0	45.5	51.2	25.0	25.1	12.0	1.00	12.0	0.932 atm
8	2/21/96	230.5	145.4	61.8	73.6	28.0	28.0	12.0	1.00	12.0	0.030 atm

Experimental Configuration

The tests are conducted inside of a stainless steel bell jar as shown in Figure 4. The bell jar measures approximately three feet (0.91 meter) in diameter by four feet (1.22 meter) in height and includes a small viewing port. An eyelet is welded to the top for raising and lowering the bell jar onto a stainless steel baseplate via an overhead crane located in the laboratory. The stainless steel baseplate is mounted atop a support stand as shown. A close-up view of the bell jar baseplate and support stand is provided in Figure 5. The chamber turbomolecular pump, which mates with a circular feed through in the center of the baseplate, is also visible in the figure. Together, the turbomolecular pump and a roughing pump provide operating pressures down to 1 x 10^{-6} torr. Regulated argon gas is available to back fill the chamber to conduct tests at varying pressures from just above vacuum to ambient.

A schematic of the test configuration, with the furnace mounted inside of the bell jar vacuum chamber on a circular brass adapter plate, is shown in Figure 6. The circular adapter plate is 0.25'' thick and is slightly larger than the outside diameter of the furnace support rings. In order to secure the furnace, the adapter plate has indentations matching the foot-print of the three furnace support rods. A sheet of Fiberfrax™ insulation is placed underneath the adapter plate to improve the thermal coupling between the furnace adapter plate and the vacuum chamber baseplate as well as to protect the surface finish on the chamber baseplate. Pass-through connectors are available inside the chamber to an external power supply and a thermocouple meter. A Hewlett Packard power supply is used to drive the furnace through two power leads attached to the heater core. The power supply has analog current and voltage gauges and is operated manually. Typically, the power supply voltage and current are set once at the beginning of a test although it is possible to override the settings to compensate for changes in the resistance of the heater as the furnace warms to operating temperature or to compensate for voltage and current instabilities in the furnace heater core. Four thermocouples are attached to the test article to measure the temperature of the furnace core, inner and outer radial shields, and the bottom end shield. Additional thermocouples are placed externally to measure the temperature of the bell jar and the ambient temperature inside the laboratory. A six channel Omega thermocouple meter is used to measure the temperature at the six thermocouple locations. The thermocouple channel is manually selected on the meter and the six temperature measurements, as well as power supply voltage and current, are recorded every quarter hour during the experiments.

Two identical power cables are attached to the furnace heater core as shown in Figure 7. Due to the high temperature of the furnace, each power cable is divided into two segments with the first, relatively short, segment attached directly to the furnace heater element. The second segment spans the distance from the end of the first segment to the pass through connector to the power supply that is located outside of the chamber. A stainless steel connector with a circular eyelet is crimped onto the end of the high temperature segment of the power cable that is attached

directly to the furnace core. A screw, through the eyelet and a graphite washer, is used to attach the power cables to threaded holes in the heater. The high temperature segment of the power cable is 20 gage stranded zinc-copper alloy wire. The power cables exit through two penetrations in the bottom end shields of the furnace. A ceramic sleeve and a high temperature resistant braided fabric are utilized to electrically insulate the power cable from exposed metallic surfaces on the furnace and adapter plate. The two power cable segments are joined by a hollow brass connector. The two wires are fed into opposite ends of the connector and secured by screws located at each end. The second segment is standard 22 gauge Teflon coated copper wire. The distance between brass connector to the power cable pass-throughs located in the center of the baseplate is approximately 16 inches.
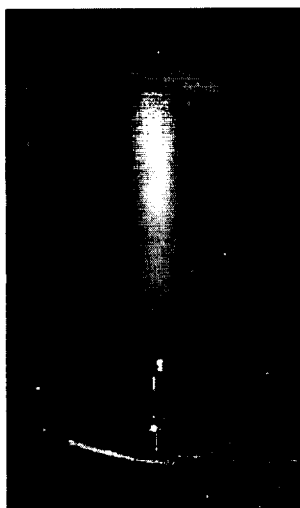

Figure 4 Stainless Steel Bell Jar

The primary thermocouple connection to measure the temperature of the furnace is through a penetration in the core. The 0.005 inch (0.127 mm) diameter thermocouple type K (chromel-alumel) leads are twisted together and inserted into the sample port of the furnace. The type K thermocouples are rated for temperatures up to 1260°C with an accuracy of +/- 0.75% between 277°C and 1260°C and +/- 4% below 277°C [13]. The thermocouple leads are electrically insulated by a ceramic sleeve that is also inserted into the sample port. The ceramic sleeve extends approximately one inch (25.4 mm) above the outer top end shield of the furnace.

After the ceramic sleeve, each lead is isolated from any electrically conducting surfaces with a braided high temperature resistant fabric insulator.
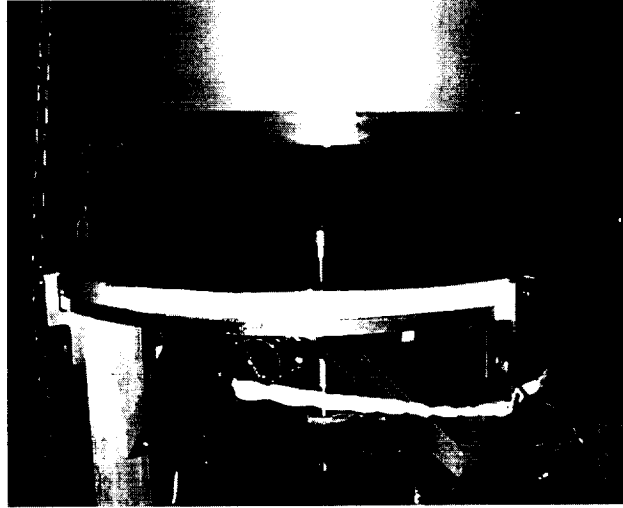

Figure 5 Close-up of the Bell Jar Baseplate and Support Stand

Two thermocouples are attached to the inner and outer radial shields of the furnace. A copper wire, utilized in conjunction with a stainless steel spring, is used to hold the thermocouples onto the outer surface of each radial shield. The spring is used to maintain tension as the copper wire expands at elevated furnace temperatures. The ends of the thermocouple wires are twisted together and looped several times between the copper wire and the radial shield. Braided fabric sleeves are used as an electrical insulator to prevent shorts between the thermocouples and metallic components of the furnace.

Vacuum Bell Jar

Chamber
Thermocouple

Feed Through
Connectors

Adapter Plate
Fiber-Frax Insulation

Baseplate

To Gas Shut-off Valve/
Supply Regulator

Hewlett Packard Power Supply

45.6

Omega DP460 6 Channel Meter

Ambient
Temperature
Thermocouple

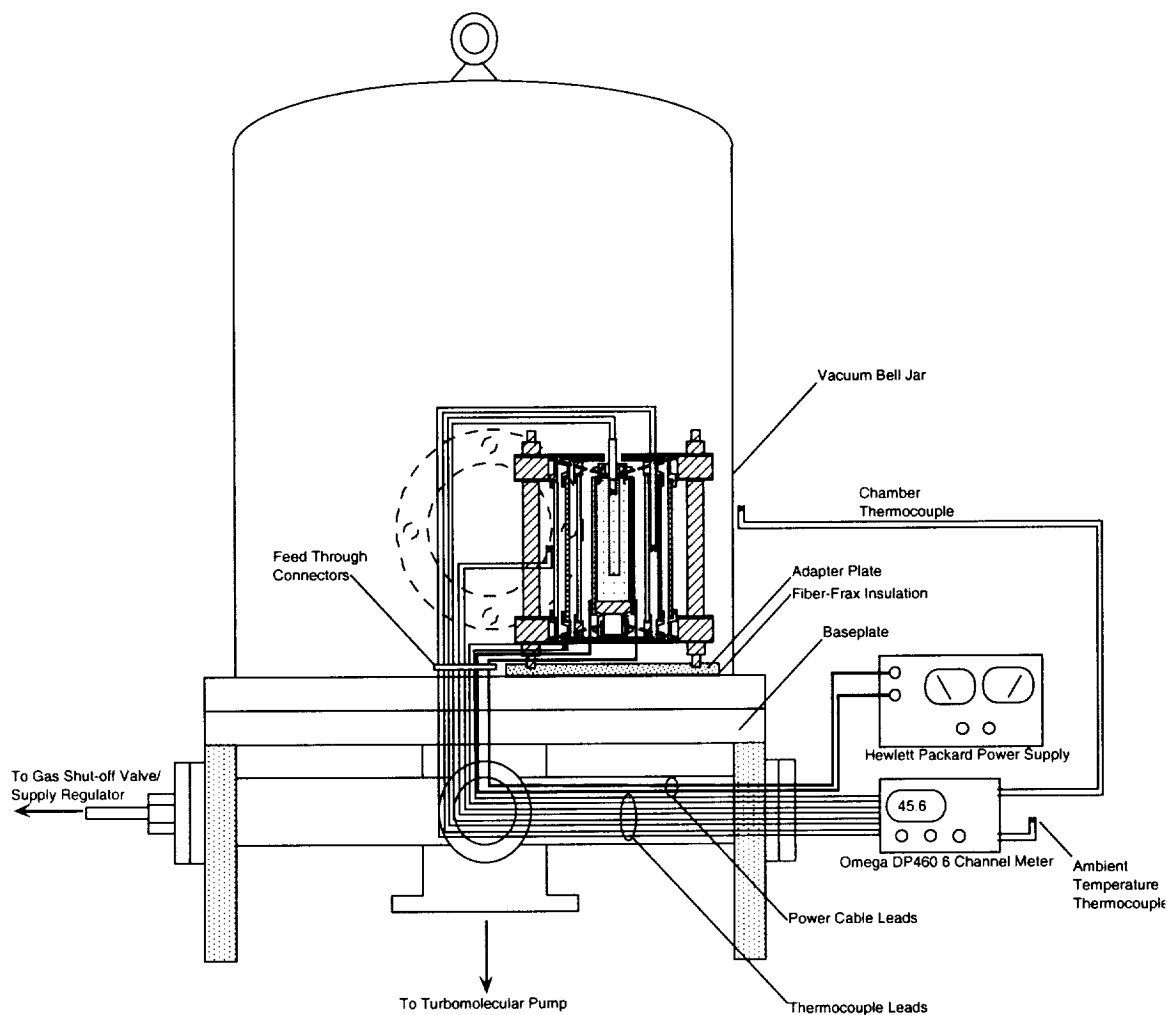Power Cable Leads

To Turbomolecular Pump

Thermocouple Leads

Figure 6 Test Setup

The final thermocouple connection is made to the outer end shield on the bottom of the furnace. The thermocouple leads are wrapped around a screw that is used to attach the bottom outer end shield to the bottom outer end ring of the furnace. As in the other connections, braided ceramic fabric sleeves are used to electrically insulate the thermocouple leads.
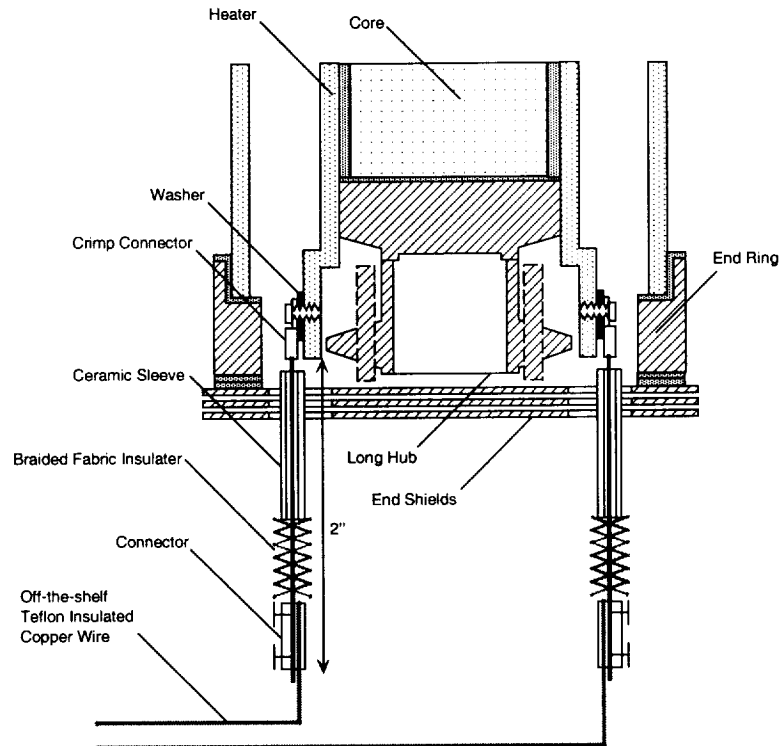
Figure 7 Power Cable Connections to the Heater Core

THERMAL MODEL

A cut-away view of the TRASYS furnace model is presented in Figure 8. Since TRASYS is only used to model planar surfaces, many of the solid elements present in the furnace, such as the core and radial shields, are constructed by defining a volume with the available planar surface primitives. Thin solid elements, such as the end shields, are modeled directly using the planar surface primitives. By using planar surfaces to model opaque solid elements, only the exterior of each planar surface is declared active within TRASYS. Inactive surfaces, such as the interior of the radial shields and end rings, are shown shaded yellow in the figure. Many of the surfaces are subdivided at common junctions with other surfaces (good practice to avoid view factor problems) or as necessary to support proper nodalization under SINDA.

The core (green) and attached long and short hubs (orange) are shown in the figure. The core is modeled using a cylindrical surface subdivided into twelve rings axially with disk surfaces to close out each end. The disks are subdivided into three rings radially to match the footprint of the attached hubs and the thickness of the boron nitride heater element. The outer envelope of each hub is modeled using a combination of cylinders and cones.
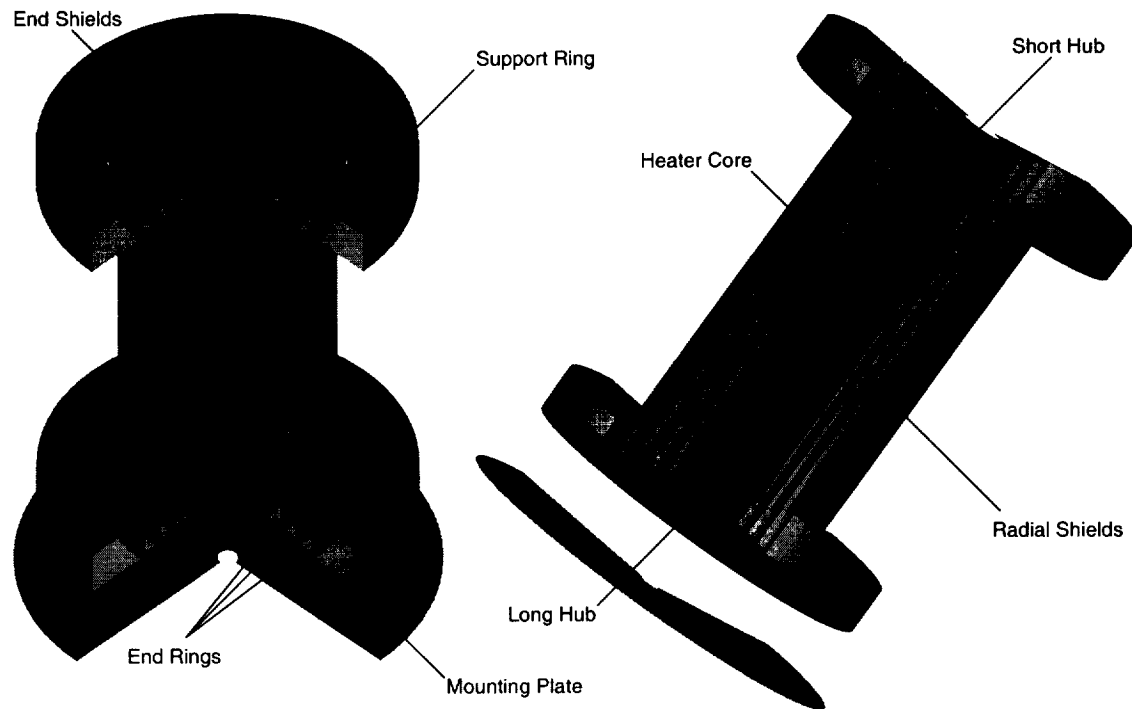
Figure 8 Cut-Away View of TRASYS Furnace Model

Like the core, the end rings (magenta) are modeled with a combination of TRASYS disk and cylinder surface primitives. The primitives are used to form the rectangular cross section shown in the figure. The disk surfaces on top of the end rings are subdivided to match the footprint of the radial shields. Cylindrical surfaces define the radial faces of the end rings. The inactive surfaces (on the inside of the end rings) are shown in yellow. The end shields (blue) are modeled using disk surfaces (that are active on both sides) and are subdivided to match the footprint of the end rings. The support rings (magenta) and radial shields (red) are modeled using cylinders for the exterior faces and disk surfaces for the top and bottom close-outs. The

radial shields, end rings, and end shields are positioned to maintain proper clearance as determined by the Fiberfrax™ washers and spacers. As shown in the figure, the inside surfaces of the cylinders and disks forming the support rings and radial shields are not active in the TRASYS model.

The support rods are not assumed to be significant contributors to the radiation exchange between the outer radial shield and the environment and are not included in the TRASYS model. The three support rods have a very small surface area relative to the area of the outer radial shield and, thus, provide little blockage between the shield and the environment. The stainless steel support rods also have a much lower emittance than the uncoated surface of the Pyrex™ outer radial shield and will absorb little of the energy exchange between the outer radial shield and the environment.

Figure 9 contains a representation of the network for the thermal model. The network, containing nodes and conductors, is overlaid upon a cut-away view of the furnace in the r-z plane. Since tangential symmetry is assumed, no conductors exist in the θ direction. Diffusion and arithmetic nodes are represented as filled and open circles, respectively. Arithmetic nodes are used primarily to model exposed surfaces that participate radiatively and correspond one-to-one with the surfaces in the radiation model. Radiation couplings are not shown, but nodes with exposed surfaces that participate radiatively are indicated with two arrows. Linear conductors are represented with an electrical resistance symbol and imposed heat sources are represented with a large arrow placed directly upon the node.
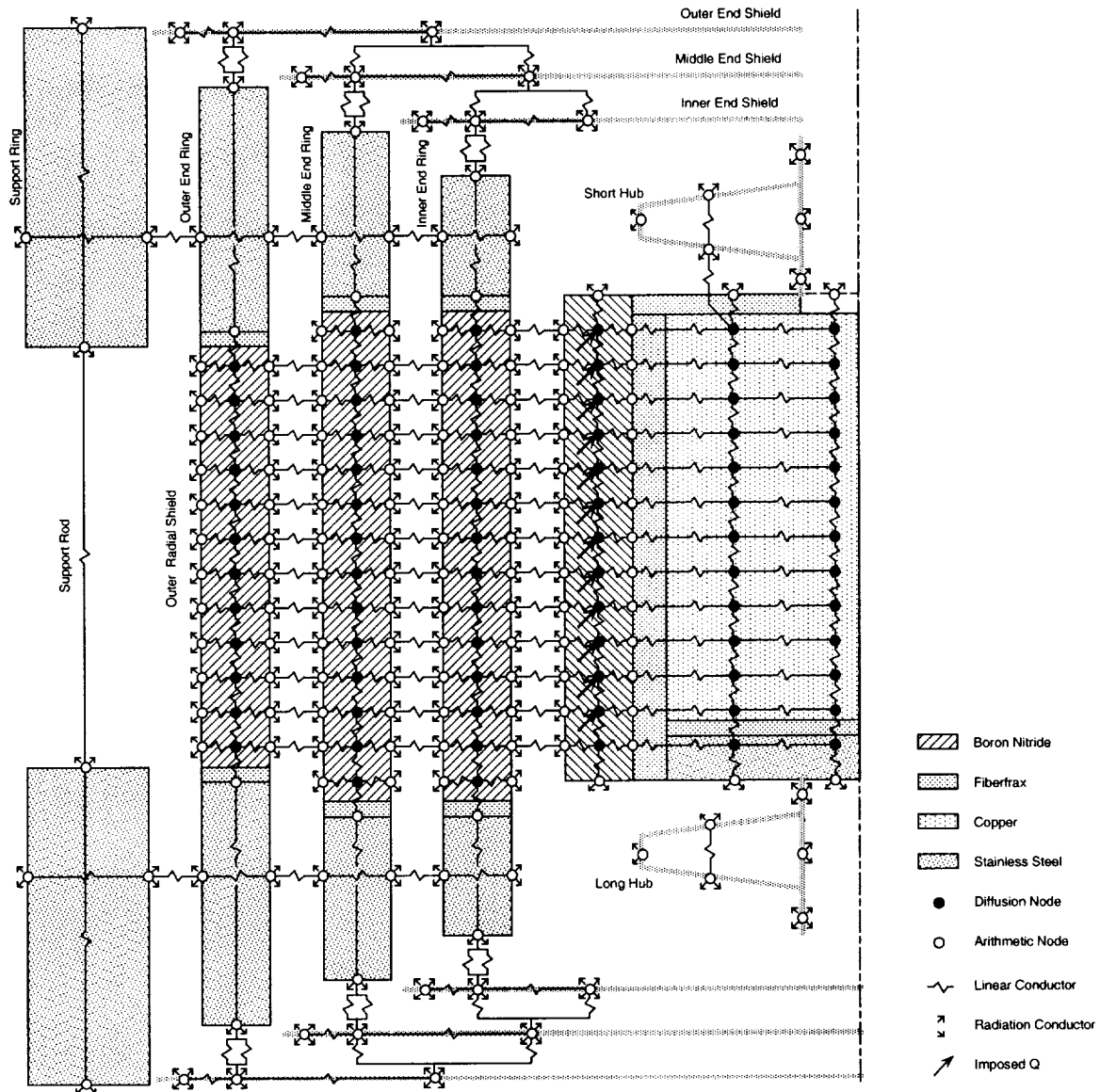
Outer End Shield

Middle End Shield

Inner End Shield

Support Ring

Outer End Ring

Middle End Ring

Inner End Ring

Short Hub

Support Rod

Outer Radial Shield

Long Hub

▨	Boron Nitride
▦	Fiberfrax
▤	Copper
▨	Stainless Steel
●	Diffusion Node
○	Arithmetic Node
⌇	Linear Conductor
⌐	Radiation Conductor
↗	Imposed Q

Figure 9 Thermal Network Model

The furnace core is discretized into a mesh of twelve diffusion nodes axially by two diffusion nodes in the radial direction. Diffusion nodes are shown as shaded blocks, arithmetic nodes are unfilled rectangles, and the geometric couplings through the core are shown italicized. In general, radial couplings between nodes in the core are computed from $2\pi L/\ln(r_o/r_i)$, where r_i and r_o are the radii to the adjacent inner and outer nodes and L is the height of the node. Axial couplings are computed by $\pi(r_o^2 - r_i^2)/L$, where r_o and r_i represent the average radii between

adjacent nodes (i.e., for node "j", $r_o=(r_{j+1}+r_j)/2$ and $r_i=(r_{j-1}+r_j)/2$) and L is the distance between nodes. The core is surrounded by Fiberfrax™ insulation and a boron nitride heater sleeve. Linear conductors are included to account for the resistance through the insulation. The heater sleeve is discretized axially to match the nodalization of the furnace core and into three nodes radially to provide surface nodes that participate radiatively with the innermost radial shield. Imposed heat sources are placed upon the heater nodes and are varied to match test conditions. Linear conductors are also included to account for the heat flow from the ends of the core into the long (bottom) and short (top) hubs. The long and short hubs exchange heat radiatively with the surroundings. Although not shown in the figure, linear conductors are included to model the support wire connections between the end hubs and the outer support rings.

The inner, middle, and outer radial shields are axially discretized into nodes that are aligned to permit conductive couplings between the shields through the gas contained in the furnace. Diffusion nodes are shown as shaded blocks, arithmetic nodes are unfilled rectangles and the geometric couplings through the Pyrex™ shields and argon gas are italicized. Gaseous conduction between the inner radial shield and the heater element is also included. To model the furnace under vacuum conditions, the gaseous conduction couplings are removed. Each shield is radially discretized into three nodes with an interior diffusion node to account for the thermal capacitance of the shield and two arithmetic nodes for the exposed inner and outer surfaces. The radial couplings are given by $2\pi L/\ln\{[(r_o+r_i)/2]/r_i\}$ and $2\pi L/\ln\{r_o/[(r_o+r_i)/2]\}$, where r_i and r_o are inner and outer radii of the radial shield and L is the height of the node. The axial couplings between adjacent nodes are computed by $\pi(r_o^2-r_i^2)/L$. Each radial shield is also conductively coupled to end rings on the top and bottom of the furnace. Since Fiberfrax™ spacers are placed between the shields and the end rings, multiple conductors are included to model the resistance of the insulation as well as gaseous conduction through the gap formed by the spacers.

A single diffusion node is used to model each end ring with arithmetic nodes on all exposed surfaces. Conductors internal to the end ring include radial and axial couplings between the diffusion node and the arithmetic nodes on the exposed surfaces. The inner and outer radial geometric couplings are computed from $2\pi L/\ln\{[(r_o+r_i)/2]/r_i\}$ and $2\pi L/\ln\{r_o/[(r_o+r_i)/2]\}$, where r_i and r_o are inner and outer radii of the end ring and L is the height. The axial couplings are computed by $\pi(r_o^2-r_i^2)/(L/2)$. The coupling between the radial shield and the end ring includes conductive paths through the Fiberfrax™ spacers and through the vapor gap formed between the end ring and radial shield. The geometric couplings for the spacer and the vapor gap are based upon the cross-sectional area of the radial shield and are computed by $\alpha\pi(R_o^2-R_i^2)/d$ and $(1-\alpha)\pi(R_o^2-R_i^2)/d$, where α is the area fraction obstructed by the spacer, d is the thickness of the spacer, and R_i and R_o are the inner and outer radii of the radial shield. The radiation coupling between the radial shield and the end ring is computed within TRASYS. Separate conductors are included to account for mounting screws that attach the end shields to the end rings, for gaseous conduction through the gap formed by the washers positioned between the end rings and the end shields, and for conduction directly through the washers. Since the screw does not contact the end shield directly, the conductive path includes radial conduction through the washer. The total coupling (washer + screw) is given by $2[2\pi d/\ln\{[(D_w+D_s)/2]/D_s\}]+(\pi D_s^2/4)/d$, where the conductive path through both washers is included. The coupling for gaseous conduction between the end ring and end shield is given by $\pi(r_f^2-r_i^2)/d$. The coupling for conduction between the end ring and the end shield through the washers is given by $[\pi(D_w^2-D_s^2)/4]/d$, where $\pi(D_w^2-D_s^2)/4$ represents the cross-sectional area of a single washer. Gaseous conduction between the end rings (in the radial direction) is also included in the model.

SPECULAR RADIATIVE EXCHANGE BETWEEN CYLINDRICAL SURFACES

Heat transfer analyses of the furnace are performed assuming diffuse radiative exchange between the surfaces of the core, the inner radial shield, and the inner end shields. The inner surface of the innermost radial shield has a low emissivity, highly specular, vacuum deposited gold coating while the end shields and the highly emissive core are non-specular. Because of the large aspect ratio (H/Δr) of the vertical annulus formed by the furnace heater core, inner radial shield, and end shields, it is assumed (in the overall TRASYS model) that the specular interchange can be approximated with a diffuse model. It is expected that only if a significant fraction of the energy radiated by the core is directly reflected onto the end shields (from the inner radial shield) is the assumption compromised.

To validate the diffuse assumption, two simplified models of the vertical annulus (formed by the core, inner radial shield, and end shields), one diffuse and one specular, are developed for comparison. The models are based upon diffuse and specular radiosity analysis methods as described by Sparrow [14]. The conclusions presented are also applicable to the vertical annuli formed by the inner and middle radial shields and the middle and outer radial shields of the furnace. These annuli differ only in geometry since the outer surfaces of the radial shields are highly emissive and non-specular like the furnace heater core.

Model Geometry

The subsequent analyses are based upon the radiative exchange between two cylinders of height, H, and inner and outer radii, r_i and r_o, respectively as shown in Figure 10. An axisymmetric coordinate system is assumed. A single ray, at height of z, is emitted from the inner cylindrical surface as shown. The emitted ray exits at angle, α, relative to the surface normal of the inner cylinder and is intercepted by the outer cylinder at an angle, β, relative to the surface normal of the outer cylinder. Since the inner and outer surface normals have no

component in the axial direction, the angles α and β are equivalent to the angle between the surface normal and the component of the ray in the r-θ plane. The elevation angle above the r-θ plane for the emitted ray is denoted φ. The elevation angle is an important parameter as the ray is specularly reflected between the surfaces of the cylinders; this angle (as well as the intercept angles α and β) is preserved on each successive specular bounce relative to the local surface normal. The end shields that close out the top and bottom ends of the vertical annulus are also shown.
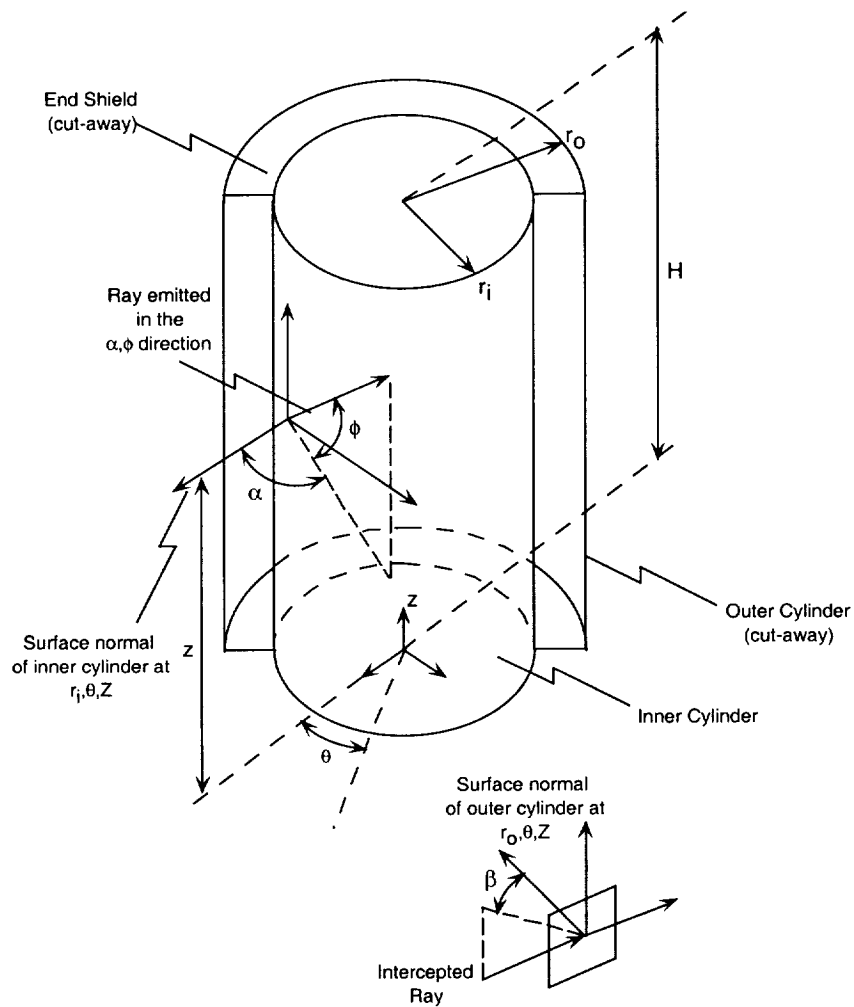
Figure 10 Axisymmetic Coordinate System

The relationship between the intercept angles α and β is shown in Figure 11. The relationship is mathematically expressed as $\beta=\sin^{-1}((r_i/r_o)\sin\alpha)$. An important characteristic for axisymmetric cylinders is that a ray emitted from the inner cylinder is always reflected back to the inner cylinder by a specular outer cylinder unless it escapes out of the annulus. The maximum intercept angle, β, for a ray emitted by the inner cylinder corresponds to $\alpha=\pi/2$ as shown in Figure 12. If a ray originating from the outer cylinder leaves at angle γ that is greater than the maximum intercept angle, the ray will bounce along the surface of the outer cylinder indefinitely, essentially orbiting the inner cylinder until it escapes from the annulus. If the elevation angle, ϕ, is exactly zero, the ray will never escape.
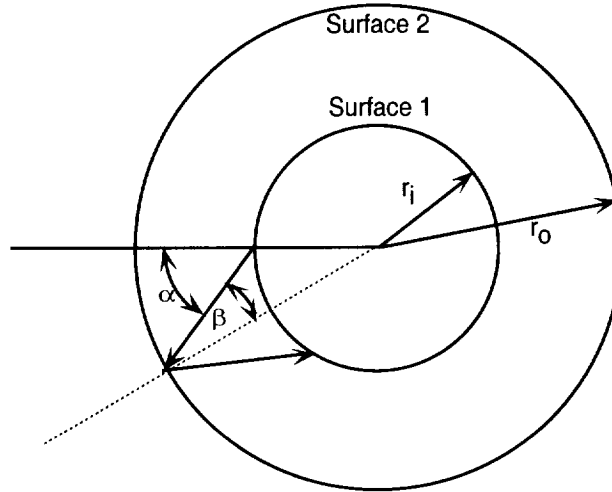

Figure 11 Relationship between Emitted and Reflected Ray

Diffuse Interchange Model

The theory behind the radiosity method [15] and its application to diffuse and specular models of a cylindrical vertical annulus are presented. An energy balance per unit area for a surface, denoted i, is provided in Figure 13. H_i is the incident flux upon the surface, $\rho_i H_i$ is the reflected incident flux, $\epsilon_i \sigma T_i^4$ is the heat flux emitted by the surface, and q_i ($=Q_i/A_i$) is the net heat gained by the surface.
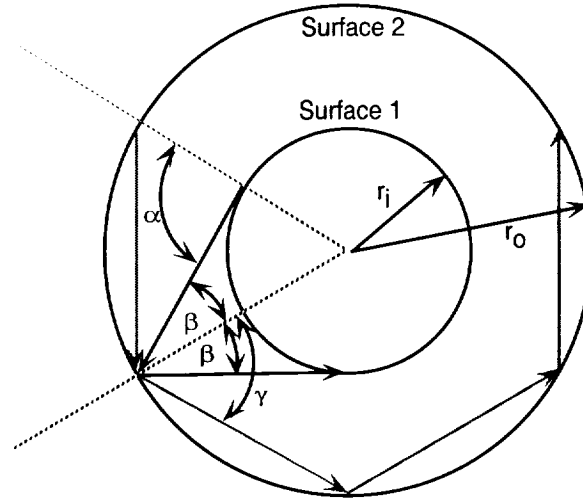
Figure 12 Emitted Ray Reflection to Inner Cylinder
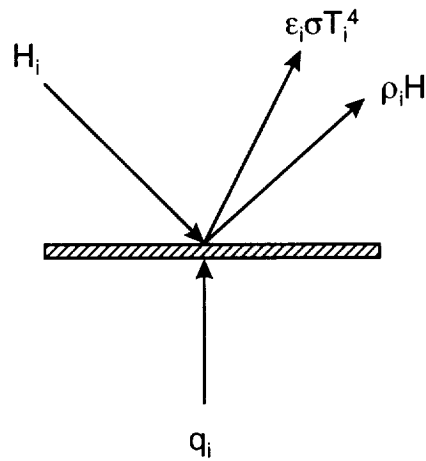

Figure 13 Energy Balance per Unit Area for a Diffusely Reflecting Surface

The radiosity of the surface, B_i, is defined as the total flux leaving the surface and is equal to the flux emitted by the surface plus the fraction of the incident flux that is reflected from the surface as shown in Equation 1.

$$B_i = \varepsilon_i \sigma T_i^4 + \rho_i H_i \tag{1}$$

In Equation 2, an energy balance is constructed where the net flux, q_i, is equal to the incident flux absorbed by the surface, $\varepsilon_i H_i$, minus the flux emitted by the surface, $\varepsilon_i \sigma T_i^4$. The net flux is equal to the rate of heat gained by the surface. Linear couplings (via conduction or convection) to other surfaces, imposed heat loads, and changes in the thermal mass of the surface are related to the net heat flux as shown in Equation 3.

$$q_i = \varepsilon_i H_i - \varepsilon_i \sigma T_i^4 \tag{2}$$

$$q_i = \frac{(mc_p)_i \dfrac{dT_i}{dt} - \sum G_{ij}(T_j - T_i) - Q_i}{A_i} \tag{3}$$

Substituting H_i from the definition of radiosity and simplifying yields an energy balance in terms of the radiosity (see Equation 4).

$$q_i = \frac{\varepsilon_i}{(1 - \varepsilon_i)}\left(B_i - \sigma T_i^4\right) \tag{4}$$

The definition of radiosity can be simplified to yield a set of equations in network form. Dividing both sides of the definition through by $(1 - \varepsilon_i)$ and then subtracting $\dfrac{\varepsilon_i B_i}{(1 - \varepsilon_i)}$ from both sides yields Equation 5.

$$B_i = \frac{\varepsilon_i}{(1 - \varepsilon_i)}\left(\sigma T_i^4 - B_i\right) + H_i \tag{5}$$

Since the radiosity, B_i, represents the heat flux leaving a surface, the incident flux upon a surface, H_i, can be found by summing the contributions from all the surfaces within the enclosure as shown in Equation 6.

$$H_i = \frac{\displaystyle\sum_{j=1}^{n} F_{ji} A_j B_j}{A_i} = \sum_{j=1}^{n} F_{ij} B_j \tag{6}$$

Since the summation of form factors from a surface is equal to 1 (Equation 7), the relation can be simplified to express the radiosity in network form (numerical differences) as shown in Equations 8 and 9.

$$\sum_{j=1}^{n} F_{ij} = 1 \tag{7}$$

$$\sum_{j=1}^{n} F_{ij} B_i = \frac{\varepsilon_i}{(1-\varepsilon_i)}\left(\sigma T_i^4 - B_i\right) + \sum_{j=1}^{n} F_{ij} B_j \tag{8}$$

$$0 = \frac{\varepsilon_i}{(1-\varepsilon_i)}\left(\sigma T_i^4 - B_i\right) + \sum_{j=1}^{n} F_{ij}\left(B_j - B_i\right) \tag{9}$$

Equations 10 and 11 are generated by multiplying through by the surface area, A_i, to express the balances in terms of rate of heat transfer rather than flux.

$$Q_i = \frac{\varepsilon_i A_i}{(1-\varepsilon_i)}\left(B_i - \sigma T_i^4\right) \tag{10}$$

$$0 = \frac{\varepsilon_i A_i}{(1-\varepsilon_i)}\left(\sigma T_i^4 - B_i\right) + \sum_{j=1}^{n} A_i F_{ij}\left(B_j - B_i\right) \tag{11}$$

The application of Equations 10 and 11 to a three surface vertical annulus is provided in Figure 14. Because of symmetry, the end shields are combined and represented by one surface. It should be noted that the single surface representing the two end shields views itself. The form factors between the surfaces within enclosure are available from the angle factor catalog in Sparrow [16].

Specular Interchange Model

A slightly different formulation is used to account for specularly reflecting surfaces within an enclosure. In the diffuse model, the energy exchange between two surfaces is directly proportional to the diffuse form factor between the surfaces. In an enclosure with one or more specular surfaces, an exchange factor is introduced to include reflected energy from specular surfaces. The exchange factor between two surfaces i and j is defined in Equation 12 where f_n is

the fraction of energy originating at surface i that arrives at surface j after n intervening specular reflections. The reflectance of an intervening specular surface, k, is given by ρ_k (which is equal to $1 - \varepsilon_k$ for a opaque surface). With each successive reflection, a fraction of the incident energy is absorbed by the specular surface. The fraction of energy for $n=0$ is the energy originating at surface i that is directly incident upon surface j and corresponds to the diffuse form factor between surfaces i and j. The energy fractions for higher order reflections can be found by the diffuse form factor between the originating surface and a reflected image of the destination surface. Determining the exchange factors in this manner becomes complex for large numbers of specular surfaces or if the specular surfaces are curved.

$$E_{ij} = f_0 + f_1\rho_k + f_2\rho_k\rho_l + \dots \tag{12}$$

With the definition of the exchange factor, the radiative heat transfer between surfaces is defined as shown in Equation 13, where N_D is the number of diffusely reflecting surfaces and N is the total number of surfaces (the specular surfaces are numbered N_D+1 through N).

$$0 = \frac{\varepsilon_i A_i}{(1-\varepsilon_i)}\left(\sigma T_i^4 - B_i\right) + \sum_{j=1}^{N_D} A_i E_{ij}\left(B_j - B_i\right) + \sum_{j=N_D+1}^{N} A_i E_{ij} \varepsilon_j (\sigma T_j^4 - B_i) \tag{13}$$

The net heat transfer rate from any of the diffusely reflecting surfaces is the same as in the diffuse formulation. Since the exchange factors already include reflections from specular surfaces, the net heat transfer from a specular surface, i, is defined as shown in Equation 14.

$$0 = \varepsilon_i A_i \left(\sigma T_i^4 - \sum_{j=1}^{N_D} E_{ij} B_j + \sum_{j=N_D+1}^{N} E_{ij} \varepsilon_j \sigma T_j^4 \right) \tag{14}$$

The application of Equations 13 and 14 to a three surface vertical annulus with the outer cylinder specularly reflecting surface is provided in Figure 15. Because of symmetry, the top and bottom end shields are combined and represented by one surface that views itself.
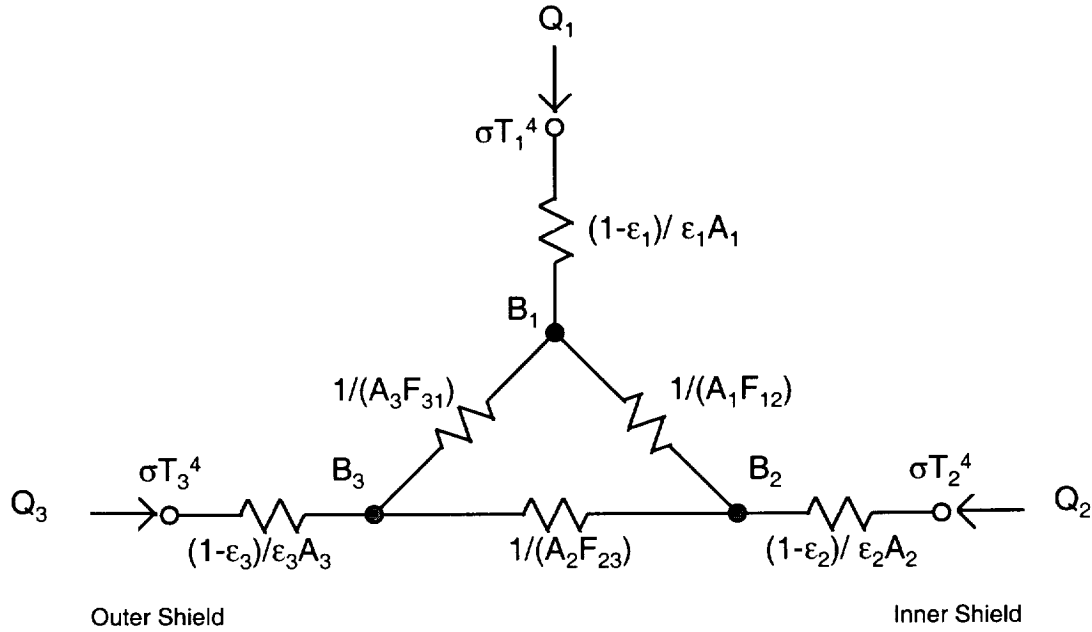
Figure 14 Radiosity Formulation for the Diffuse Model

Specular Exchange Factors

The diffuse network is easily solvable after determining the diffuse form factors from available angle factor correlations. The determination of the exchange factors contained within the specular model is more complex. For the exchange factor between surfaces 1 and 2, a ray originating from surface 2 may either be reflected back to surface 2 or reflected to surface 1. The ray may not sustain more than one intervening specular reflection before reaching surface 1 as shown in Equation 15. In Equation 16, the exchange factor E_{23} is identical to the form factor between the two surfaces since a ray emitted by surface 2 is either reflected back to surface 2 or reflected to surface 1. It is not possible for a ray originating at surface 2 to be reflected by surface 3 onto surface 3. As shown in Equation 17, it is possible for a ray emitted by surface 3 to be specularly reflected many times by surface 3 before reaching surface 1.

$$E_{21} = F_{21} + \rho_3 f_1 \tag{15}$$

$$E_{23} = F_{23} \tag{16}$$

$$E_{31} = F_{31} + \sum_{n=1}^{\infty} \rho_3{}^n f_n \qquad (17)$$

End Shields
(Diffuse)

Q_1

$\sigma T_1{}^4$

$(1-\varepsilon_1)/\varepsilon_1 A_1$

B_1

$1/(\varepsilon_3 A_3 E_{31})$ $1/(A_1 E_{12})$

$\sigma T_3{}^4$ B_2 $\sigma T_2{}^4$

Q_3 ———————————————— Q_2

$1/(\varepsilon_3 A_2 E_{23})$ $(1-\varepsilon_2)/\varepsilon_2 A_2$

Outer Shield   Inner Shield
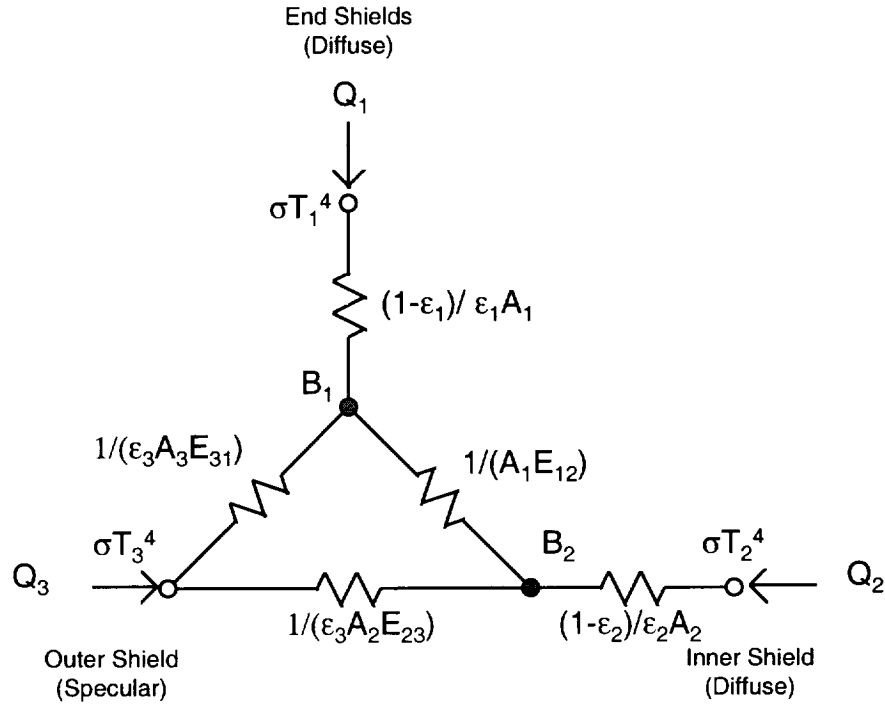(Specular)   (Diffuse)

Figure 15 Radiosity Formulation for the Specular Model

The exchange factor between the surfaces 1 and 2 (the inner cylinder and end shields) is determined by subdividing the inner cylinder into axial segments and computing diffuse form factors from each segment to the outer cylinder. Radiation emitted by the inner cylinder may follow one of three paths as shown in Figure 16. In the first path, the radiation is directly incident upon the end shields. In the second path, radiation incident upon the outer shield is reflected to one of the end shields on a single bounce. In the third path, the remaining radiation incident upon the outer shield is reflected back to the inner cylinder. This simplification is possible since no ray that is both emitted by the inner cylinder and incident upon the outer cylinder can be reflected back to the outer cylinder; the ray must return to the inner cylinder or be reflected to one of the end shields. The form factors from the inner cylinder to the outer cylinder and end shields are

either computed directly from available correlations or derived from angle factor algebra (see
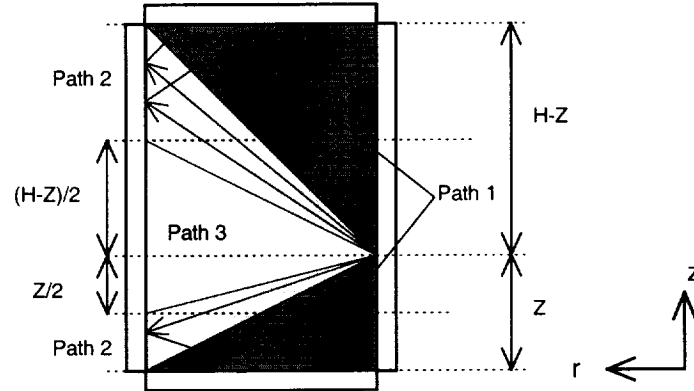
Sparrow [17]).

Figure 16 Destination of Radiation Emitted by the Inner Cylinder

The angle factor algebra necessary to determine the diffuse form factors corresponding to

ray paths 1, 2, and 3 originating from a point on the inner cylinder is shown in Figure 17. Surface

A is the originating surface and form factors to surfaces C, D, and E are desired (the form factor

to surface F is known analytically). The process is illustrated for the upper region only and can

be repeated to determine the form factors to corresponding surfaces in the lower region.

Imaginary surfaces G and H are used to facilitate the calculation. Form factors F_{AC}, F_{AD}, and

$F_{AE}+F_{AF}$ correspond to ray paths 1, 2, and 3 respectively. From analytical correlations it is

possible to determine all possible form factors within a vertical annulus formed by concentric

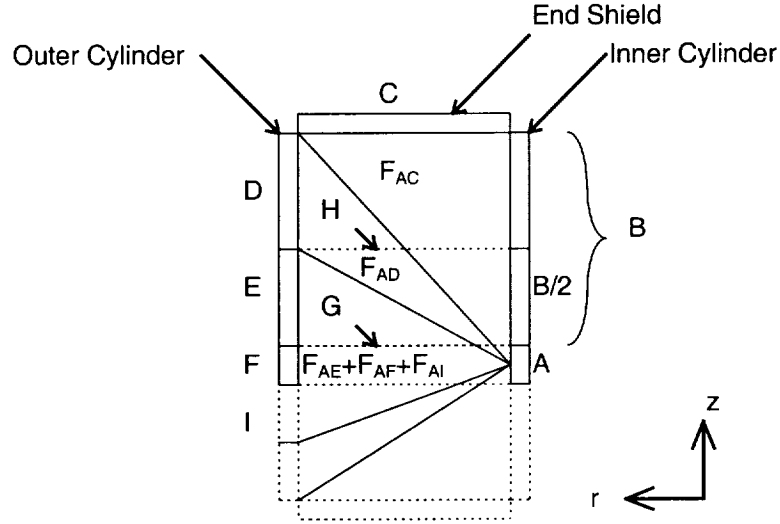cylinders of equal height. The form factors known analytically are indicated with an apostrophe.

Figure 17 Angle Factor Algebra

The form factors between surface C and surfaces B and A+B are analytically known. The form factor from surface C to A is determined as shown in Equation 18. The form factor from surface A to C can be determined through reciprocity as shown in Equation 19. The form factor from surface A to C represents the fraction of energy emitted by A that is directly incident upon C (Path 1).

$$F_{C \rightarrow A} = F'_{C \rightarrow A+B} - F'_{C \rightarrow B}$$ (18)

$$F_{A \rightarrow C} = F_{C \rightarrow A} \frac{A_C}{A_A} = \left(F'_{C \rightarrow A+B} - F'_{C \rightarrow B} \right) \frac{A_C}{A_A}$$ (19)

The form factor from surface A to the imaginary surface H can be determined in a similar manner as shown in Equations 20 and 21.

$$F_{H \rightarrow A} = F'_{H \rightarrow A + \frac{B}{2}} - F'_{H \rightarrow \frac{B}{2}}$$ (20)

$$F_{A \rightarrow H} = F_{H \rightarrow A} \frac{A_H}{A_A} = \left(F'_{H \rightarrow A + \frac{B}{2}} - F'_{C \rightarrow \frac{B}{2}} \right) \frac{A_C}{A_H}$$ (21)

Using the imaginary surface G, the form factor between surface A and surface E can be determined from the relationship in Equation 22. This is one of three form factors required to

compute the fraction of energy emitted by surface A that is directly incident upon the outer cylinder along path 3.

$$F'_{A \to G} = F_{A \to E} + F_{A \to H} \tag{22}$$

The combined view from surface A to surfaces D and E can be determined from the relationship in Equation 23 using imaginary surface G. The form factor from surface A to surface D is determined by subtracting the form factor to surface E determined previously from the combined view (Equation 24). The form factor from A to D represents the fraction of energy emitted by surface A that is reflected onto surface C from the specular outer cylinder (path 2).

$$F'_{A \to G} = F_{A \to D+E} + F_{A \to C} \tag{23}$$

$$F_{A \to D} = F_{A \to D+E} - F_{A \to E} \tag{24}$$

To determine the total diffuse form factors corresponding to the energy fractions transmitted to the outer and end shields, the inner cylinder is axially subdivided into a number of segments as shown in Figure 18. The number of axial segments is incremented until the results returned by the computation vary by less than 1×10^{-4} with 2500 and 3000 segments typical of the number of divisions used. The diffuse form factors are determined at the vertical midpoint of each segment and are then numerically integrated over the height of the cylinder to find the total diffuse form factor from the inner surface. A trapezoidal approximation is used for the integration scheme.
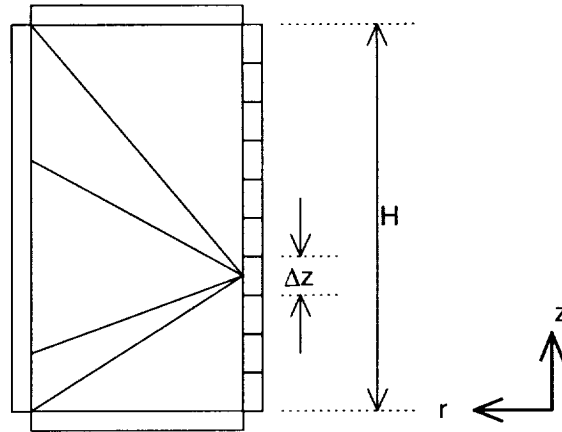
Figure 0.18 Determination of the Total Form Factors from the Inner Cylinder

The results from the computation for the geometry corresponding to the vertical annulus between the furnace heater core and inner radial shield are presented in Table 4.2. The total form factor between the core and end shields is almost doubled due to specular reflections from the inner radial shield. The results are checked by summing the form factors from the core to the end shield via reflection from the inner radial shield and to the inner radial shield. The sum should equal the analytically calculated diffuse form factor of 0.96187 between concentric cylinders which it does as shown.

Table 4.2 Results of the Form Factor Calculations

From Surface	To Surface	Mode	Form Factor
Core	End Shields	Direct	0.03813
Core	End Shields	Reflection	0.03762
Core	Inner Radial Shield	Direct	0.92425
Sum			1.00000

Determining the exchange factor between surfaces 3 and 1 (the outer radial shield and the end shield) is complicated by the curvature of surface 3. Since surface 3 has a nonzero view of itself ($F_{33} \sim 0.25$), rays originating from surface 3 can be reflected many times before reaching the end shield (surface 1). This phenomenon is shown in Figure 19 for two different rays originating from surface 3.
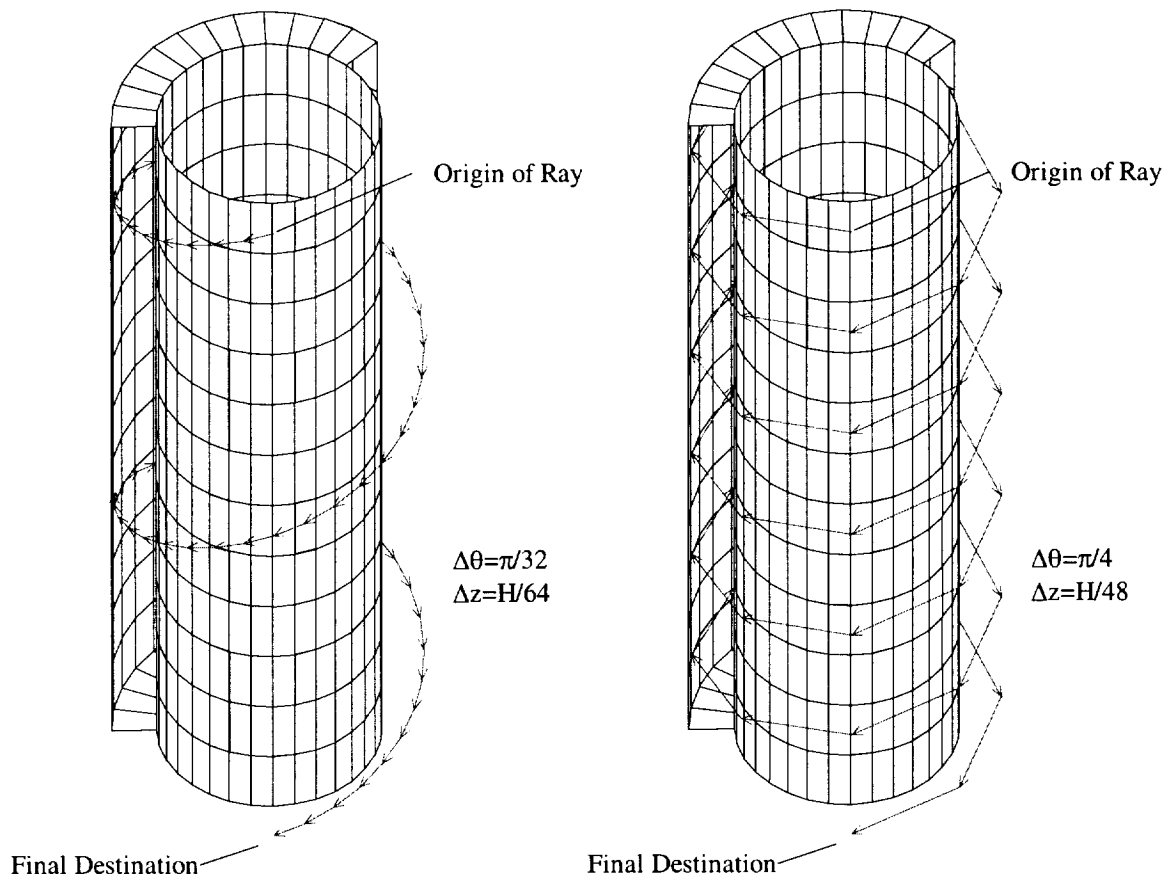

Figure 19 Anatomy of a Specular Reflection

Fortunately, no ray originating from surface 3 can be reflected by surface 3 onto surface 2. The indirect portion of the exchange factor between surfaces 3 and 1 is determined by numerically integrating the product of the diffuse form factor from surface 3 to itself multiplied by the reflectance raised to the integer number of bounces before reaching surface 1. Equation 25

represents the exchange factor between an infinitesimal area on surface 3 to surface 1. To obtain the total exchange factor between surface 3 and surface 1, the infinitesimal exchange factor is integrated over the entire area of surface 3 as shown in Equation 26. Definitions for the angles β_i and β_j and the segment r_{ij} connecting the two areas are illustrated in Figure 20.

$$(\rho_3^n f_n)_{dA_i \to A_j} = \int_{A_j} \frac{\rho_3^n \cos\beta_i \cos\beta_j dA_j}{\pi r^2} \tag{25}$$

$$\sum_{n=1}^{\infty} \rho_3{}^n f_n = \frac{1}{A_i} \int_{A_i} (\rho_3^n f_n)_{dA_i \to A_j} dA_i \tag{26}$$
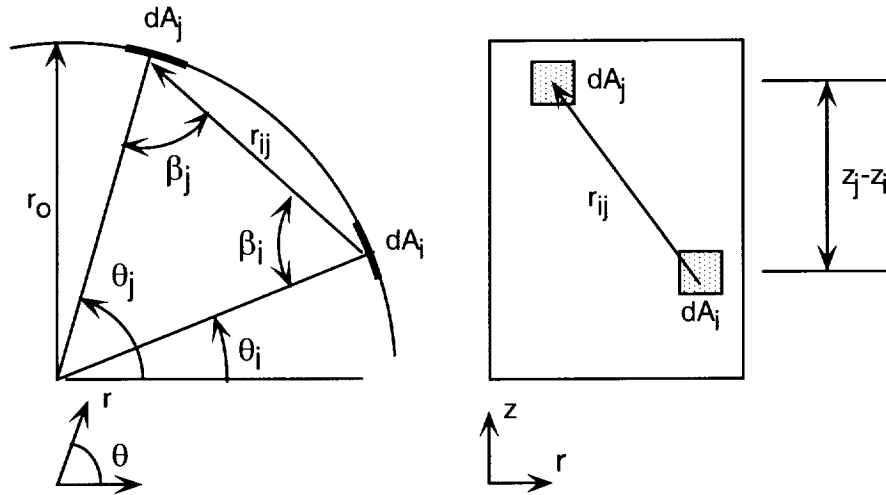

Figure 20 Form Factor Calculation Parameters

The exchange factor equations are simplified with the following definitions (in Equations 27, 28, and 29) for r_{ij}, $\cos\beta_i$, and $\cos\beta_j$, where $\vec{n}_i$ and $\vec{n}_j$ are the surface normals for the infinitesimal surfaces.

$$r_{ij} = \sqrt{(x_j - x_i)^2 + (y_j - y_i)^2 + (z_j - z_i)^2}$$

$$= \sqrt{r_o^2(\cos\theta_j - \cos\theta_i)^2 + r_o^2(\sin\theta_j - \sin\theta_i)^2 + (z_j - z_i)^2}$$

$$= \sqrt{r_o^2(2 - 2\cos\theta_j\cos\theta_i - 2\sin\theta_j\sin\theta_i) + (z_j - z_i)^2} \qquad (27)$$

$$= \sqrt{2r_o^2(1 - (\cos\theta_j\cos\theta_i - \sin\theta_j\sin\theta_i)) + (z_j - z_i)^2}$$

$$= \sqrt{2r_o^2(1 - \cos(\theta_j - \theta_i)) + (z_j - z_i)^2}$$

$$\cos\beta_i = \vec{n}_i \cdot \frac{\vec{r}_{ij}}{|r_{ij}|} = \left(-\cos\theta_i\hat{i} - \sin\theta_i\hat{j}\right) \cdot \frac{\left((\cos\theta_j - \cos\theta_i)\hat{i} + (\sin\theta_j - \sin\theta_i)\hat{j} + (z_j - z_i)\hat{k}\right)}{\sqrt{2r_o^2(1 - \cos(\theta_j - \theta_i)) + (z_j - z_i)^2}}$$

$$= \frac{r_o\left(\cos(\theta_j - \theta_i) - 1\right)}{\sqrt{2r_o^2(1 - \cos(\theta_j - \theta_i)) + (z_j - z_i)^2}} \qquad (28)$$

$$\cos\beta_j = \vec{n}_j \cdot \frac{\vec{r}_{ij}}{|r_{ij}|} = \left(-\cos\theta_j\hat{i} - \sin\theta_j\hat{j}\right) \cdot \frac{\left((\cos\theta_j - \cos\theta_i)\hat{i} + (\sin\theta_j - \sin\theta_i)\hat{j} + (z_j - z_i)\hat{k}\right)}{\sqrt{2r_o^2(1 - \cos(\theta_j - \theta_i)) + (z_j - z_i)^2}}$$

$$= \frac{r_o\left(\cos(\theta_j - \theta_i) - 1\right)}{\sqrt{2r_o^2(1 - \cos(\theta_j - \theta_i)) + (z_j - z_i)^2}} \qquad (29)$$

The final form of the integral over surface A_j is given in Equation 30. The exponent n, which is the integer number of reflections before a ray originating at A_i reaches the upper or lower end shield, is determined by dividing the distance from z_i to the upper or lower end shield by the difference in height between A_i and A_j. Which end shield is the final destination of the ray is determined by height of A_j relative A_i (e.g., if A_j is below A_i the ray will be reflected to the lower end shield).

$$(\rho_3^n f_n)_{dA_i \to A_j} = \int_{A_j} \rho_3^n \frac{r_o^2\left(\cos(\theta_j - \theta_i) - 1\right)^2}{\pi\left(2r_o^2(1 - \cos(\theta_j - \theta_i)) + (z_j - z_i)^2\right)^2} dA_j \qquad (30)$$

The infinitesimal surface area dA_j is equal to $r_o d\theta dz$. The limits for integration in the axial direction are from 0 to the height of the cylinder. The integration limits in the circumferential direction correspond to the unobstructed view that an infinitesimal area on the

surface of the outer cylinder has of the outer cylinder. The half angle is illustrated in Figure 21

by a ray that just misses the inner cylinder. If the origin of the ray is set to $\theta=0$, the limits of

integration are +/- $(\pi-2\beta)$. The angle β of the grazing ray is equal to $\sin^{-1}(r_i/r_o)$.
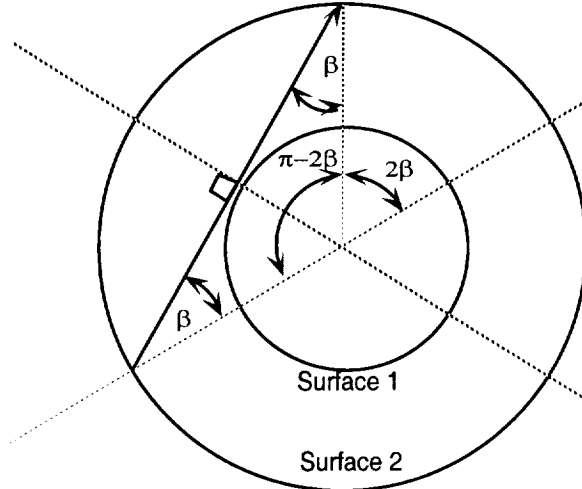

Figure 21 Integration Limits for Form Factor Integration

The final form of the integral to determine the exchange factor from dA_i to A_j is

provided in Equation 31.

$$(\rho_3^n f_n)_{dA_i \to A_j} = \int_0^H \rho_3^n \int_{-(\pi-2\beta)}^{+(\pi-2\beta)} \frac{r_o^2 (\cos(\theta_j - \theta_i) - 1)^2}{\pi (2r_o^2 (1 - \cos(\theta_j - \theta_i)) + (z_j - z_i)^2)^2} r_o d\theta dz \tag{31}$$

Since the view of dA_i to A_j is dependent upon height only, the final form of the total

integral can be expressed as shown in Equation 32.

$$\sum_{n=1}^{\infty} \rho_3^n f_n = \frac{1}{A_i} \int_{A_i} (\rho_3^n f_n)_{dA_i \to A_j} dA_i = \frac{1}{H} \int_0^H (\rho_3^n f_n)_{dA_i \to A_j} dz \tag{32}$$

The formulation is checked by substituting a reflectance of 1.0 for surface 3. If surface 3

is ideally reflective, the fraction of energy emitted by surface 3 that is incident upon the end

shield (surface 1) should be identical to the diffuse form factor between surface 3 and itself.

From analytical correlations, the diffuse form factor $F_{33}=0.24132$. Evaluating the expression above with a reflectance of 1 yields an energy fraction of 0.23944, a difference of less than 1%. The actual fraction of energy emitted by surface 3 that is specularly reflected onto the end shield is 0.21121.

The exchange factors for the specularly reflecting model are calculated as shown in Equations 33, 34, and 35.

$$E_{21} = F_{21} + \rho_3 f_1 = 0.03813 + 0.97 \times 0.03762 = 0.074621 \tag{33}$$

$$E_{23} = F_{23} = 0.96187 \tag{34}$$

$$E_{31} = F_{31} + \sum_{n=1}^{\infty} \rho_3{}^n f_n = 0.05692 + 0.21121 = 0.26813 \tag{35}$$

Solution and Results

The governing equations for the diffuse and specularly reflecting models are written in matrix form and solved. The governing equations for the diffusely reflecting three surface model are provided in Equations 36 and 37.

$$
\begin{bmatrix} Q_1 \\ Q_2 \\ Q_3 \end{bmatrix} = \sigma \begin{bmatrix} \dfrac{\varepsilon_1 A_1}{1-\varepsilon_1} & 0 & 0 \\ 0 & \dfrac{\varepsilon_2 A_2}{1-\varepsilon_2} & 0 \\ 0 & 0 & \dfrac{\varepsilon_3 A_3}{1-\varepsilon_3} \end{bmatrix} \left(\begin{bmatrix} B_1 \\ B_2 \\ B_3 \end{bmatrix} - \begin{bmatrix} T_1^4 \\ T_2^4 \\ T_3^4 \end{bmatrix} \right) \tag{36}
$$

$$
\begin{bmatrix} 0 \\ 0 \\ 0 \end{bmatrix} = \sigma \begin{bmatrix} \dfrac{\varepsilon_1 A_1}{1-\varepsilon_1} & 0 & 0 \\ 0 & \dfrac{\varepsilon_2 A_2}{1-\varepsilon_2} & 0 \\ 0 & 0 & \dfrac{\varepsilon_3 A_3}{1-\varepsilon_3} \end{bmatrix} \left(\begin{bmatrix} T_1^4 \\ T_2^4 \\ T_3^4 \end{bmatrix} - \begin{bmatrix} B_1 \\ B_2 \\ B_3 \end{bmatrix} \right) + \sigma \begin{bmatrix} -A_1(F_{12}+F_{13}) & A_1 F_{12} & A_1 F_{13} \\ A_2 F_{21} & -A_2(F_{21}+F_{23}) & A_2 F_{23} \\ A_3 F_{31} & A_3 F_{32} & -A_3(F_{31}+F_{32}) \end{bmatrix} \begin{bmatrix} B_1 \\ B_2 \\ B_3 \end{bmatrix} \tag{37}
$$

It is possible to solve for the radiosity in terms of temperature as shown in Equations 38 and 39.

$$\begin{bmatrix} \dfrac{\varepsilon_1 A_1}{1-\varepsilon_1} & 0 & 0 \\[2mm] 0 & \dfrac{\varepsilon_2 A_2}{1-\varepsilon_2} & 0 \\[2mm] 0 & 0 & \dfrac{\varepsilon_3 A_3}{1-\varepsilon_3} \end{bmatrix} \begin{bmatrix} T_1^4 \\ T_2^4 \\ T_3^4 \end{bmatrix} = \begin{bmatrix} \dfrac{\varepsilon_1 A_1}{1-\varepsilon_1} + A_1(F_{12}+F_{13}) & -A_1 F_{12} & -A_1 F_{13} \\[2mm] -A_2 F_{21} & \dfrac{\varepsilon_2 A_2}{1-\varepsilon_2} + A_2(F_{21}+F_{23}) & -A_2 F_{23} \\[2mm] -A_3 F_{31} & -A_3 F_{32} & \dfrac{\varepsilon_3 A_3}{1-\varepsilon_3} + A_3(F_{31}+F_{32}) \end{bmatrix} \begin{bmatrix} B_1 \\ B_2 \\ B_2 \end{bmatrix} \tag{38}$$

$$\begin{bmatrix} T_1^4 \\ T_2^4 \\ T_3^4 \end{bmatrix} = \begin{bmatrix} 1 + \dfrac{1-\varepsilon_1}{\varepsilon_1}(F_{12}+F_{13}) & -\dfrac{1-\varepsilon_1}{\varepsilon_1}F_{12} & -\dfrac{1-\varepsilon_1}{\varepsilon_1}F_{13} \\[2mm] -\dfrac{1-\varepsilon_2}{\varepsilon_2}F_{21} & 1 + \dfrac{1-\varepsilon_2}{\varepsilon_2}(F_{21}+F_{23}) & -\dfrac{1-\varepsilon_2}{\varepsilon_2}F_{23} \\[2mm] -\dfrac{1-\varepsilon_3}{\varepsilon_3}F_{31} & -\dfrac{1-\varepsilon_3}{\varepsilon_3}F_{32} & 1 + \dfrac{1-\varepsilon_3}{\varepsilon_3}(F_{31}+F_{32}) \end{bmatrix} \begin{bmatrix} B_1 \\ B_2 \\ B_2 \end{bmatrix} \tag{39}$$

Substituting for the radiosity yields the final matrix form for the diffuse model as shown in Equation 40.

$$\begin{bmatrix} Q_1 \\ Q_2 \\ Q_3 \end{bmatrix} = \sigma \begin{bmatrix} \dfrac{\varepsilon_1 A_1}{1-\varepsilon_1} & 0 & 0 \\[2mm] 0 & \dfrac{\varepsilon_2 A_2}{1-\varepsilon_2} & 0 \\[2mm] 0 & 0 & \dfrac{\varepsilon_3 A_3}{1-\varepsilon_3} \end{bmatrix} \left(\begin{bmatrix} 1 + \dfrac{1-\varepsilon_1}{\varepsilon_1}(F_{12}+F_{13}) & -\dfrac{1-\varepsilon_1}{\varepsilon_1}F_{12} & -\dfrac{1-\varepsilon_1}{\varepsilon_1}F_{13} \\[2mm] -\dfrac{1-\varepsilon_2}{\varepsilon_2}F_{21} & 1 + \dfrac{1-\varepsilon_2}{\varepsilon_2}(F_{21}+F_{23}) & -\dfrac{1-\varepsilon_2}{\varepsilon_2}F_{23} \\[2mm] -\dfrac{1-\varepsilon_3}{\varepsilon_3}F_{31} & -\dfrac{1-\varepsilon_3}{\varepsilon_3}F_{32} & 1 + \dfrac{1-\varepsilon_3}{\varepsilon_3}(F_{31}+F_{32}) \end{bmatrix}^{-1} - [I] \right) \begin{bmatrix} T_1^4 \\ T_2^4 \\ T_3^4 \end{bmatrix} \tag{40}$$

The governing equations for the specularly reflecting three surface model are provided in Equations 41 and 42.

$$\begin{bmatrix} Q_1 \\ Q_2 \\ Q_3 \end{bmatrix} = \begin{bmatrix} \dfrac{\varepsilon_1 A_1}{1-\varepsilon_1} & 0 \\[2mm] 0 & \dfrac{\varepsilon_2 A_2}{1-\varepsilon_2} \\[2mm] \varepsilon_3 A_3 E_{31} & \varepsilon_3 A_3 E_{32} \end{bmatrix} \begin{bmatrix} B_1 \\ B_2 \end{bmatrix} - \sigma \begin{bmatrix} \dfrac{\varepsilon_1 A_1}{1-\varepsilon_1} & 0 & 0 \\[2mm] 0 & \dfrac{\varepsilon_2 A_2}{1-\varepsilon_2} & 0 \\[2mm] 0 & 0 & \varepsilon_3 A_3(E_{31}+E_{32}) \end{bmatrix} \begin{bmatrix} T_1^4 \\ T_2^4 \\ T_3^4 \end{bmatrix} \tag{41}$$

$$\begin{bmatrix} \dfrac{\varepsilon_1 A_1}{1-\varepsilon_1} + A_1 E_{12} + \varepsilon_3 A_1 E_{13} & -A_1 E_{12} \\[2mm] -A_2 E_{21} & \dfrac{\varepsilon_2 A_2}{1-\varepsilon_2} + A_2 E_{21} + \varepsilon_3 A_2 E_{23} \end{bmatrix} \begin{bmatrix} B_1 \\ B_2 \end{bmatrix} = \sigma \begin{bmatrix} \dfrac{\varepsilon_1 A_1}{1-\varepsilon_1} & 0 & \varepsilon_3 A_1 E_{13} \\[2mm] 0 & \dfrac{\varepsilon_2 A_2}{1-\varepsilon_2} & \varepsilon_3 A_2 E_{23} \end{bmatrix} \begin{bmatrix} T_1^4 \\ T_2^4 \\ T_3^4 \end{bmatrix} \tag{42}$$

After defining the matrices O, P, R, and S, the specular relations are rewritten as shown in Equations 43 and 44. The final matrix form for the solution of the specularly reflecting problem is derived in Equation 45.

$$\begin{bmatrix} Q_1 \\ Q_2 \\ Q_3 \end{bmatrix} = [P]\begin{bmatrix} B_1 \\ B_2 \end{bmatrix} - \sigma[O]\begin{bmatrix} T_1^4 \\ T_2^4 \\ T_3^4 \end{bmatrix} \tag{43}$$

$$[R]\begin{bmatrix} B_1 \\ B_2 \end{bmatrix} = \sigma[S]\begin{bmatrix} T_1^4 \\ T_2^4 \\ T_3^4 \end{bmatrix} \tag{44}$$

$$
\begin{bmatrix} Q_1 \\ Q_2 \\ Q_3 \end{bmatrix} = \sigma \left(OR^{-1}S - P \right) \begin{bmatrix} T_1^4 \\ T_2^4 \\ T_3^4 \end{bmatrix}
$$

(45)

The diffuse and specular model results are shown parametrically in Table 4.3 for three furnace power levels. The heat rate is applied to the surface representing the inner cylinder. The outer cylinder and end shield are radiatively coupled to a boundary node representing the environment. The geometry and emissivities of the surfaces are chosen to be representative of the vertical annulus formed by the furnace heater core and inner radial shield. These results are based upon simplified models and are intended for comparison only.

Table 4.3 Results from the Diffuse and Specular Analyses

	Q_2=8.0 Watts			Q_2=4.0 Watts			Q_2=1.0 Watt		
	Diffuse °C	Specular °C	Delta °C	Diffuse °C	Specular °C	Delta °C	Diffuse °C	Specular °C	Delta °C
Core	626.4	639.5	-13.1	486.4	497.3	-10.9	276.1	283.3	-7.2
End Shield	527.4	525.0	2.3	404.4	402.5	1.9	222.9	221.7	1.2
Inner Radial Shield	537.4	539.4	-2.0	412.7	414.3	-1.6	228.2	229.2	-1.0

CONCLUSIONS

The specular surface of the outer cylinder (inner radial shield) does not appear to significantly influence the temperatures of either the end shield(s) or the inner radial shield relative to a diffuse outer surface. However, a specular outer cylinder results in a significantly warmer core. This result is not intuitively obvious since specular reflections from the inner radial shield would seem to reflect more heat to the ends of the furnace, which are less resistant to radiative heat leak to the environment (higher emissivity). However, the radial resistance to heat flow is much greater with a specular shield as demonstrated in Figure 22. With a diffuse outer surface, energy emitted by the core that is incident upon the inner radial shield is diffusely reflected back to the core with a form factor of only 0.7. Approximately 65% of the heat emitted

by the core is reflected back to the core on the first exchange with the remainder diffusely reflected to the inner radial shield or to the end shield(s). With a specular shield, approximately 90% of the energy emitted by the core is returned to the core by specular reflections where it is readily absorbed by the highly emissive surface. This is both an unexpected and important result because it appears to be supported by the test data. Measured differences in temperature between the core and inner radial shield are greater than what are predicted by the diffuse assumptions in the overall furnace model.
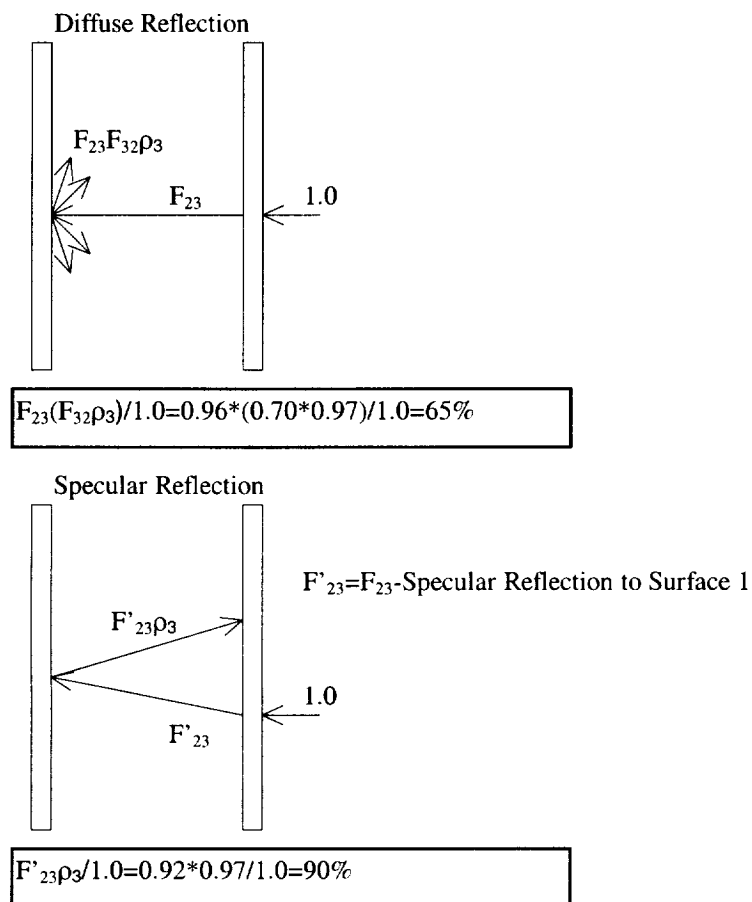

Figure 22 Diffuse and Specular Reflections